PERGAMON

International Journal of Heat and Mass Transfer 45 (2002) 1965–1982

International Journal of HEAT and MASS TRANSFER

www.elsevier.com/locate/ijhmt

Scalar transport in a quasi two-dimensional turbulent wake interacting with a boundary layer

G.A. Sideridis, E.G. Kastrinakis, S.G. Nychas *

Department of Chemical Engineering, Aristotle University of Thessaloniki, Univ. Box 453, 54006 Thessaloniki, Greece

Received 30 December 2000

Abstract

An experimental study of heat transport in the interaction region between the wake of a cylinder and a turbulent boundary layer is presented in this work. The cylinder was placed parallel to a flat plate and normal to the flow. Its position was selected above the boundary layer edge, so that the lower part of the wake was interacting with the boundary layer. Heat was supplied to the boundary layer flow by means of a line heat source. Presence of surface roughness on the cylinder resulted in the deviation of the velocity power spectrum scaling region from the $-5/3$ power law which is characteristic of three-dimensional turbulence. Point measurements of the instantaneous values of two velocity components and temperature have been taken using hot-wire anemometry. Two turbulent scalar flux components and a Reynolds shear stress component have been obtained directly from the experimental data. Results were assessed in conjunction with the periodic coherent structures in the wake (a von Kármán vortex street) using a phase-averaging technique that provided a clear picture of the heat transport procedures involved.

1. Introduction

Mass transfer between interacting flows is an issue of primary importance in many engineering applications and in environmental flows. It is related directly to processes like heating and cooling, progress of a chemical reaction, aerodynamic behavior and also, to atmospheric dispersion of gaseous pollutants, etc. Mass transfer is the direct result of entrainment and mixing phenomena taking place in the interaction region. The mechanism that produces such phenomena is associated to the particular features of the interacting flows. It has been established that entrainment originates primarily from large-scale engulfment and the subsequent mixing and diffusion are related to small-scale perturbations [1,2]. In the present experimental work, the wake of a circular cylinder was interacting with a turbulent boundary layer on a flat plate. The large-scale, highly organized structures inside the wake, the von Kármán street of vortices, are expected to play a major role in the entrainment process. They also have a significant impact on mixing and diffusion because they are involved with intensive turbulence production due to vortex stretching [3]. Hussain and Hayakawa [4] investigated extensively the topological features and properties of adjacent von Kármán vortices and proposed a detailed model for this flow.

For the complex flow of a cylinder wake interacting with a turbulent boundary layer, the limited number of experimental works published refer usually to the case of a cylinder totally immersed in the boundary layer (classified as a "boundary layer manipulator", [5,6]). However, numerical simulations of vortex interactions with solid surfaces have received more attention [7–9]. Usually in numerical studies, a single two-dimensional vortex is considered, traveling in a free-stream and passing closely to a wall, interacting with the boundary layer. Reliable experimental validation of such numerical methods is not feasible because of the difficulty in producing in the laboratory an isolated two-dimensional vortex. Usually, a von Kármán street of vortices is generated, which has a quasi two-dimensional character, but essentially, it is three-dimensional. The term two-dimensional flow implies that one fluctuating velocity component is suppressed compared to the other two (in

* Corresponding author.

0017-9310/02/$ - see front matter
PII: S0017-9310(01)00287-3

the case of a von Kármán vortex street, the velocity component parallel to the axis of the cylinder). Another flow characteristic associated with two-dimensionality is the deviation of the scaling region of the velocity power spectrum from the $-5/3$ power law, which is characteristic of isotropic, three-dimensional turbulence. The classical theoretical result for two-dimensional turbulence is -3 [10,11]. Typical examples of real flows with distinctive two-dimensional turbulence characteristics are the atmospheric flow at high altitude (above the earth's boundary layer) and the sea currents in the open oceans. In these cases, velocity variations are significant only on horizontal planes of motion, but not in the vertical direction. An extensive discussion on two-dimensional real flows may be found in [11].

The original motivation for the present experimental work was the simulation in a wind tunnel of quasi two-dimensional environmental flows. Furthermore, such a simulation can serve for a qualitative validation of related numerical models. For that reason, particular effort was given to enhancing the two-dimensional character of the wake in the present flow.

Experimental results, obtained in an earlier investigation of ours, have been used here for that purpose (some results have been presented by Sideridis et al. [12]). It has been observed that if the Reynolds number based on the cylinder's diameter D is within the range $1500 < R_D < 3000$, the velocity power spectrum scaling region deviates from the $-5/3$ power law in the intermediate wake ($20 < x/D < 40$). Using a cylinder with rough surface at the same R_D values, the range for scaling region deviation expands to $10 < x/D < 40$. Hence, in the present work, R_D was chosen close to 2000 and a circular cylinder covered with sandpaper was used (details about the experimental conditions will be given in the next section).

The spanwise velocity component $w(t)$ has not been measured systematically. A few exploratory measurements in the wake indicated a 30% lower rms value compared to the other two velocity components. The significant presence of $w(t)$ implies that there might be important three-dimensional effects present in the flow. It is noted here that the present experimental configuration in its final form may also be used for the simulation of flows in numerous practical situations, in addition to the environmental flows mentioned earlier. For example, the flow behind a tube in an engineering apparatus, the surface of which has been deformed by some chemical action (e.g., excessive corrosion, deposition of chemical substances, etc.). Similarly, the flow downstream of an underwater pipe, installed parallel to the sea bed, the surface of which has been colonized by marine life.

Mass transport in complex flows like the present one, is difficult to be measured directly. It can be simulated, however, by heat transport based on the fact that the Prandtl and Schmidt numbers for gases are both close to one. Consequently, the mass and heat diffusivities are of the same order. In the present flow, heat was supplied to the boundary layer flow by a line heat source (details are given in the next section) and it is traced through the interaction region. Present analysis of experimental data is an extension of the analysis presented in Sideridis et al. [13]. That work resulted in the determination of the particular directions along which heat was transferred towards the wake. The present analysis is focused on the investigation of the role of the wake coherent motion in the heat transport process.

2. Experimental procedure

An open–return, suction-type wind tunnel was used for the present experimental work. The size of the test section was $0.3 \times 0.3 \times 2$ m^3 and the free-stream turbulence level was less than 0.4%. The experimental set-up for the present measurements is shown in Fig. 1(a). The flat plate with sharp leading edge and rounded tip was installed in the test section with its top surface parallel to the main flow in order to avoid flow separation phenomena. The boundary layer was tripped near the leading edge for fully turbulent flow development along the plate. The type of the tripping device was that suggested by Hama [14]. It consisted of a row of thin triangular patches pasted on the surface of the plate. As Hama showed in his paper, a spiral motion was promoted in the space between neighboring triangles, producing continuous three-dimensional vortex shedding. Tripping was occurring in a very short distance, without significant interference effects to the boundary layer flow.

The cylinder with diameter $D = 7.6$ mm was placed at a distance h_c from the surface of the plate equal to $5D$. As the local boundary layer thickness was $\delta_0 \approx 3D$, the ratio h_c/δ_0 is approximately equal to 1.6. Therefore, the von Kármán vortex street initiated at a location in the free stream well above the boundary layer edge, but close enough for interaction to occur at a streamwise distance from the cylinder of about $10D$.

The surface temperature of the electrically heated wire providing heat to the boundary layer flow was estimated to 150 °C. It was producing a peak temperature rise at the measurement station of about 1.5 °C. The flat plate surface remained at isothermal conditions, at ambient temperature.

All measurements presented here were taken using hot-wire anemometry. The triple-wire probe shown schematically in Fig. 1(b) was used. It was formed by an X-type double-wire probe for the measurement of the streamwise and vertical velocity components and a single (cold)-wire probe for the simultaneous recording of the instantaneous temperature. It was operated by a multi-channel anemometer unit, type AN-1003 of A.A.

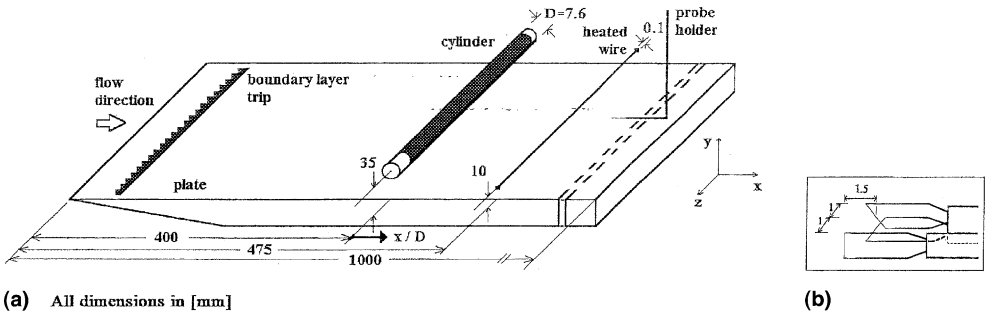

Fig. 1. (a) The experimental set-up for the present measurements, (b) schematic presentation of the triple-wire probe used.

Lab Systems. The anemometer unit output signals were digitized by an 8-channel, 16-bit analog to digital converter, type Data Translation DT-2809. The sampling frequency was 4 kHz and 163 800 samples were recorded per channel. Digital signals were then supplied to a personal computer for processing. The computer program used was developed with the LabVIEW programming software of National Instruments Corporation.

A brief description of the triple-wire probe calibration procedure is given below (a detailed report of the technique can be found in Papanicolaou et al. [15]). The probe was placed near the exit of an electrically heated jet of air. Keeping the jet velocity at the exit constant, the electric power supplied to the heating device was increased in steps. As soon as the jet reached a steady state after each increment, the cold-wire output voltage was recorded and plotted against the jet temperature provided by a thermocouple. The cold-wire calibration law (a straight line) was thus determined. For the calibration of the hot-wire X-probe, the jet was heated gradually, at constant mass flow rate monitored by a flowmeter located upstream of the heating element. Electrical power was supplied to the jet-heating element gradually in order to raise the jet temperature about 10 °C, over a period of 10 min. During this period, the cold- and hot-wire outputs were recorded simultaneously. The jet temperature was evaluated using the cold-wire calibration law. The corresponding jet velocity was then determined as follows. First, the flowmeter indication was recorded and the corresponding jet velocity at the current ambient temperature was obtained from the flowmeter calibration curve. Assuming atmospheric pressure at the jet exit and applying the perfect gas law in the form $\rho_{(T)} = (T_a/T)\rho_{(T\alpha)}$ (where ρ = air density, T = jet temperature (in K) and suffix α denotes ambient conditions), the jet velocity at the current jet temperature, $U_{(T)}$ can be evaluated as shown below.

Since

$$U_{(T\alpha)} = \frac{\dot{m}}{\rho_{(T\alpha)}A}, \quad U_{(T)} = \frac{\dot{m}}{\rho_{(T)}A}, \tag{1}$$

where $\dot{m}$ is the air mass flow rate (recorded by the flowmeter), A is the cross-sectional area at the exit of the jet,we have

$$\frac{U_{(T)}}{U_{(T\alpha)}} = \frac{\rho_{(T\alpha)}}{\rho_{(T)}} \tag{2}$$

and therefore

$$U_{(T)} = U_{(T\alpha)}\frac{T}{T_\alpha}. \tag{3}$$

The procedure was repeated at several jet mass flow rates, thus providing a hot-wire calibration databank covering a predetermined temperature range.

During the present experiments, the triple-wire probe recorded simultaneously at any point, the streamwise and the vertical velocity components $U(t) = \overline{U} + u(t)$, $V(t) = \overline{V} + v(t)$ and temperature $T(t) = \overline{T} + T'(t)$ (an overbar denotes overall time-averaged values and a lower case letter or a prime, denotes fluctuations). The estimated error in the measurement of the velocity components and temperature was $\pm 2.5\%$ and $\pm 1\%$, respectively. The heat flux components $uT'(t)$ and $vT'(t)$ and the momentum flux $uv(t)$ were also evaluated, by a digital post-processing methodology. The estimated error in these calculations was of the order of $\pm 4\%$. The nominal free-stream velocity was $U_0 = 3.5$ m/s, which gives $R_D = 1820$. The friction velocity U_τ, referred to the plate and obtained from a $(U_0 - U_{(y)})/U_\tau$ vs. y/δ_0 Clauser plot, was $U_\tau = 0.175$ m/s.

The turbulent Prandtl number Pr_t

$$\left(= \frac{\text{eddy diffusivity of momentum}, \varepsilon_m}{\text{eddy diffusivity of heat}, \varepsilon_h} \right)$$

has been evaluated using the following relations for $\varepsilon_m, \varepsilon_h$:

$$\varepsilon_m = -\frac{\overline{uv}}{d\overline{U}/dy}, \quad \varepsilon_h = -\frac{\overline{vT'}}{d\overline{T}/dy}. \tag{4}$$

A representative value for Pr, t for the present flow is 1.4.

The turbulent Reynolds number R_λ, based on the Taylor's microscale λ (estimated to 3.4 mm) was found

equal to 820 for the present flow. The length λ was obtained from the relation

$$\lambda = \left[\frac{\overline{u^2}}{\overline{(\partial u/\partial x)^2}} \right]^{1/2}. \quad (5)$$

Using Taylor's hypothesis

$$\left[\frac{\partial}{\partial x} = \frac{-1}{\overline{U}} \left(\frac{\partial}{\partial t} \right) \right],$$

relation Eq. (5) simplifies to

$$\lambda = \left[\overline{u^2} \frac{\overline{U^2}}{\overline{(\partial u/\partial t)^2}} \right]^{1/2}. \quad (6)$$

The probe was traversed from a point well within the free stream to a distance of 4 mm from the surface of the plate, at the locations: $x/D = 15$, 25 and 35.

3. Results

3.1. The mean flow

Typical profiles of the streamwise mean velocity $\overline{U}/U_0$ for the present flow are plotted in Fig. 2(a) against the normalized distance from the plate y^+ ($= U_\tau y/\nu$, where $\nu = 1.465 \times 10^{-5}$ m^2/s, the kinematic viscosity of air). The streamwise mean velocity distribution at $x/D = 25$, normalized by the friction velocity U_τ is plotted in Fig. 2(b) against y^+ on a logarithmic scale and compared to a logarithmic law, typical of fully turbulent boundary layer flow. Also shown in Fig. 2(b) is the mean velocity distribution at the same x/D location with the cylinder removed, i.e., without the wake. It is evident from Fig. 2(b) that the mean velocity distribution in the free boundary flow case coincides with the logarithmic law, denoting fully turbulent flow. Its momentum thickness has been found equal to 2 mm and the Reynolds number based on that equal to 500. The complete configuration velocity profile follows the logarithmic law in its lower part, in the boundary layer region, whereas in its upper part, it displays a well-defined velocity defect, as expected within the wake of the cylinder.

Fig. 2(c) presents mean temperature profiles normalized by the ambient temperature T_0. In Fig. 2(d) the complete configuration $\overline{T}/T_0$ distribution at $x/D = 25$ is compared to the corresponding mean temperature distribution in the free boundary layer. The complete configuration profile has a lower peak, shifted to higher y^+ values, thus indicating the important role the cylinder wake plays in the vertical heat transport.

The maximum mean velocity defect U_d and the maximum mean temperature excess T_e, which will be used later for normalization, are defined at every x/D station as follows: $U_d = U_0 - U_{min}$ (U_{min} = minimum velocity in the wake, refer to Fig. 2(a)), $T_e = T_{max} - T_0$ (T_{max} = maximum temperature behind the heated wire, refer to Fig. 2(c)). Values of U_d/U_0 and $T_e = T_0$ for the present flow are given in Table 1.

Profiles of the root-mean-square values of the streamwise and vertical velocity components in the present flow are shown in Figs. 3(a) and (b), respectively. The continuous reduction with downstream distance of peak values in the wake region is expected and attributed to the weakening of the coherent vortices [16]. The irregularities in the profiles in Fig. 3(a) near $y^+ = 170$ (which are significant at $x/D = 15$, but non-existing at $x/D = 35$) are due to the presence of the thermal wake behind the heating wire. In both Figs. 3(a) and (b), all complete configuration profiles coincide with the typical free boundary layer profile close to the plate ($y^+ < 100$), thus indicating the extent of the influence of the wake to the boundary layer flow.

The r.m.s. temperature profiles for the wake–boundary layer configuration (Fig. 3(c)) show clearly the progressive spreading of heat in the vertical direction, as a result of the interaction between the two flows. Fig. 3(d) supports this argument, where a complete configuration profile and a free boundary layer profile at $x/D = 25$ are compared.

3.2. Velocity power spectral characteristics

As mentioned in Section 1, a specific aim of the present work was the enhancement of the quasi two-dimensional characteristics of the cylinder wake flow by establishing experimental conditions at which the velocity power spectra would follow a power law with exponent other than $-5/3$. This was accomplished by using a cylinder with rough surface and selecting a value for the Reynolds number within the range $1500 < R_D < 3000$ (i.e., $R_D = 2000$). The effect on the vertical velocity power spectral density (PSD) distribution appears in Fig. 4(a). At experimental conditions other than the above (e.g., $R_D = 4000$, smooth surface) the velocity power spectrum is typical of a three-dimensional flow: a scaling region exists with constant slope equal to $-5/3$. At the specific conditions $R_D = 2000$, rough surface, there is a clear decrease of the slope of the scaling region, i.e., there is a deviation from the $n = -5/3$ power law to one with higher negative exponent.

Fig. 4(b) shows a typical normal velocity power spectrum distribution in the wake of the present flow ($n = 0$ curve). This curve displays two distinct features: (a) a peak at the Strouhal frequency ($= S_t U_0/D = 97$ Hz, where $S_t = 0.21$, the Strouhal number), thus indicating the presence of strong von Kármán vortices, and (b) a scaling region starting just after the peak frequency. The following method has been used for the determination of the slope of the scaling region [17]. The ordinates of the

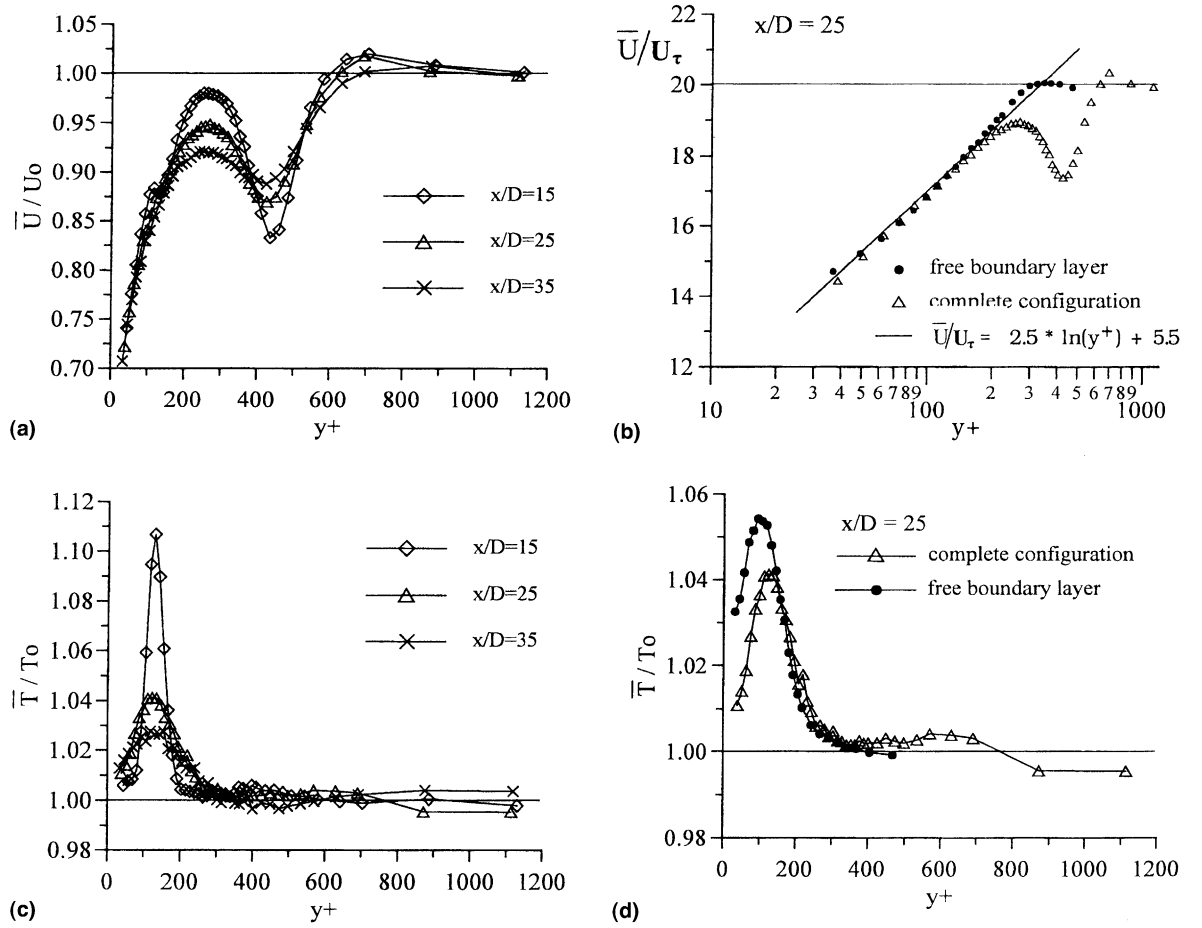

Fig. 2. (a), (c) Mean velocity and temperature profiles along the vertical direction for the combined wake–boundary layer flow. (b), (d) Comparison with the free boundary layer case at $x/D = 25$.

spectrum distribution curve were multiplied by f^n, where f denotes the corresponding values of frequency and n, the anticipated slope of the scaling region. The effect of this transformation is that the part of the spectrum that follows a power law with exponent $-n$ appears horizontal. The values $n = 5/3$ and $n = 3$ have been considered in Fig. 4(b). It is evident that the scaling region of the normal velocity spectrum starts with a short section with slope $-5/3$ (in the range 100–250 Hz) which is followed by a main section (in the range 250–800 Hz) with slope close to -3, the theoretical value for two-dimensional turbulence.

Table 1
Values of maximum mean velocity defect, U_d, maximum mean temperature excess, T_e and vortex convection velocity, U_v, at the measurement stations

x/D	U_d/U_0	T_e/T_0	U_v/U_0
15	0.169	0.108	0.915
25	0.130	0.041	0.935
35	0.111	0.027	0.944

The velocity PSD distribution in Fig. 4(b) has been obtained at the first measurement station, the one closest to the cylinder ($x/D = 15$). Hence, the spectrum peak and the extent of the scaling region with slope -3 are most noticeable. At larger x/D values the spectrum peak is lower and the frequency range of the scaling region of interest is shorter; at $x/D = 35$, it is 300–650 Hz (Fig. 4(c)). Both events reflect the weakening of the large-scale von Kármán vortices with streamwise distance and the resulting dominance of the small-scale, three-dimensional fluctuations in the flow.

3.3. The coherent flow

One of the dominant features of the present flow is the presence of the von Kármán vortices in the wake. Their main characteristics are: (a) a large-scale coherent nature (hence the term coherent flow refers to the flow field

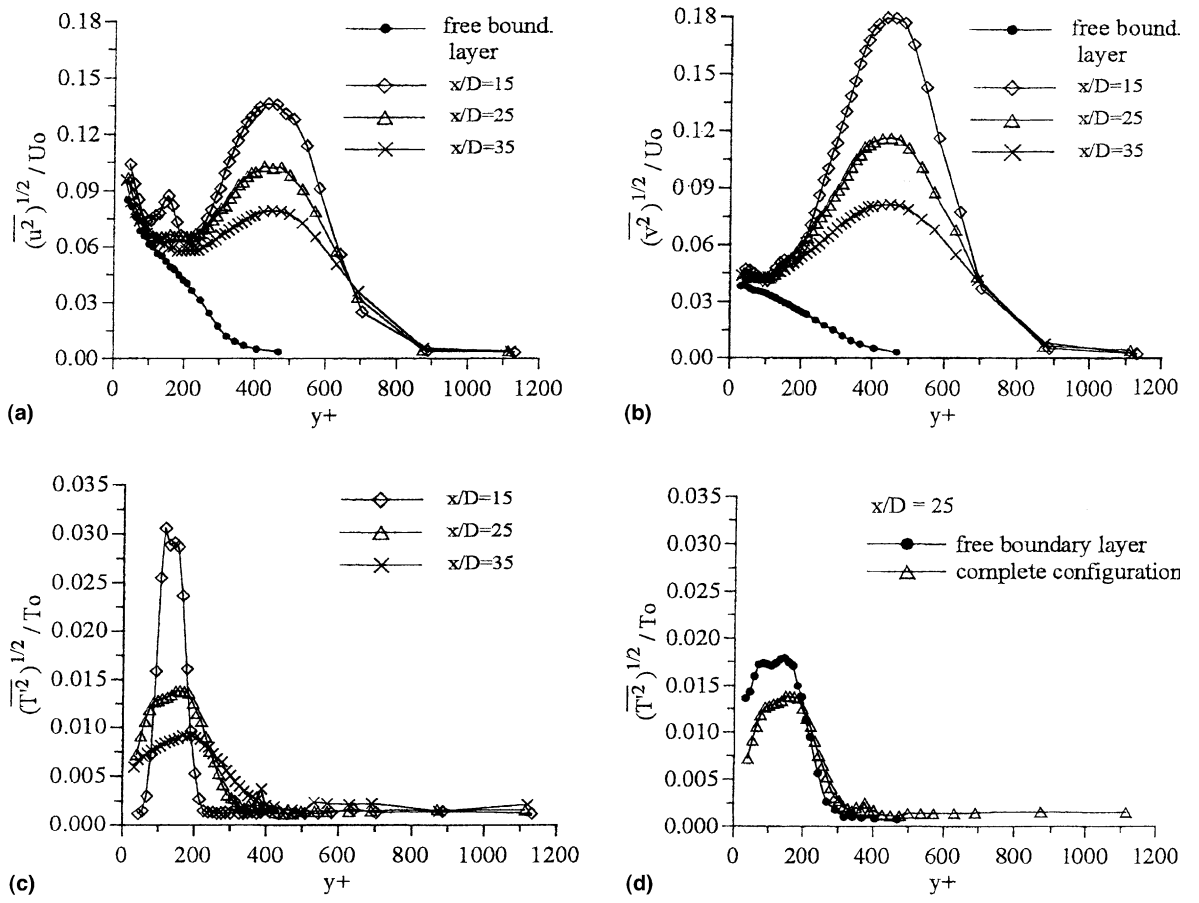

Fig. 3. Profiles of the r.m.s. values of the streamwise and vertical velocity components and temperature for both the wake–boundary layer and the free boundary layer configurations.

associated with these structures), (b) steady shedding frequency, (c) small dispersion in transverse location, strength and shape, and (d) production of large normal velocity fluctuations $v(t)$, especially near the center of the wake [3,6]. Hence, a coherent structures education method may not necessarily be based on the instantaneous vorticity distribution, as the vortical nature of the structures implies, but on a phase-averaging technique utilizing a conditioning signal derived from the time history of $v(t)$. In the present work, a phase-averaging method similar to that used by Matsumura and Antonia [16] and Kiya and Matsumura [18] was adopted. A brief description is presented in the following section.

3.3.1. The phase-averaging methodology

The stability of the shedding frequency and the small dispersion of the coherent vortices permitted the use of the local (at the measurement point) $v(t)$ signal in order to increase the sensitivity and accuracy of the education method. This signal was initially band-pass filtered with the center frequency of the filter adjusted at the von Kármán vortex-shedding frequency, f_s. The value of f_s was obtained from the normal velocity power spectrum peak (typical power spectra for the present flow have been shown in Fig. 3). The filter output signal $v_f(t)$ was used as a reference signal for the detection of the time instants satisfying simultaneously both conditions $v_f(t) = 0$ and $dv_f/dt > 0$. These instants mark on the time-scale the starting points of the vortex-shedding periods (the average distance between two consecutive points is equal to the average vortex-shedding period, $T_s = 1/f_s$). Each shedding period was divided into 40 classes of equal width (= 9°, or $\pi/20$ rad). Next, a phase time signal $\phi(t)$ was created with values ranging from 0 to 2π, having $\phi(t) = 0$ at the beginning and $\phi(t) = 2\pi$ at the end of each shedding period. It is noticed here that $v(t)$ and $\phi(t)$ as well as the time signal of any other parameter measured, e.g., $Q(t)$ ($\equiv U(t)$, $V(t)$, $T(t)$) are all synchronous time signals with the same time length (= sampling period = 40.95 s). Hence, every instant in $Q(t)$ corresponds to an instant in $\phi(t)$, and furthermore, every point of signal $Q(t)$ falls into one of the 40 classes

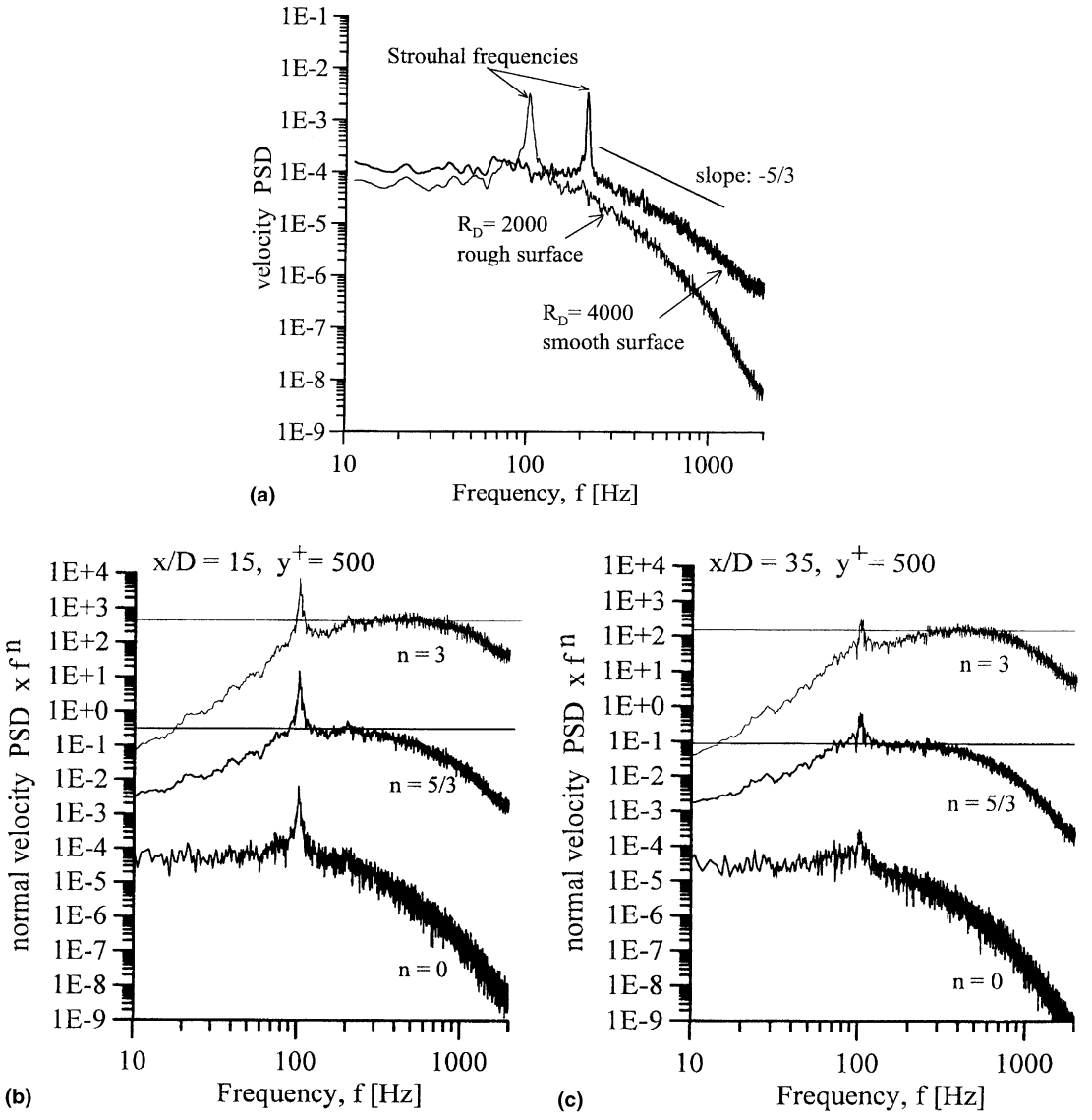

Fig. 4. (a) Effect of Reynolds number R_D and cylinder surface roughness on the normal velocity power spectral density distribution in the intermediate wake of an isolated cylinder in a free stream at $x/D = 15$. (b) Typical normal velocity power spectrum in the wake of the present flow ($n = 0$ curve). Determination of sections in the scaling region which follow a $-5/3$ power law ($n = 5/3$ curve) and a -3 power law ($n = 3$ curve). $x/D = 15$, $y^+ = 500$. (c) Normal velocity power spectrum at $x/D = 35$, $y^+ = 500$.

assumed for $\phi(t)$. All $Q(t)$ points that corresponds to the same $\phi(t)$ class were ensemble-averaged, thus providing a single value for that $\phi(t)$ class. The collection of values for all classes provides the phase-averaged distribution of the parameter $Q(t)$ over a shedding period. Phase-averaged results refer to the periodic component of the original signal $Q(t)$, because any random component disappears by definition. Hence, the application of a phase-averaging method implies that

$$Q(t) = \overline{Q} + q_c + q_r, \tag{7}$$

i.e., the original signal $Q(t)$ consists of a time-mean value $\overline{Q}$, a periodic (coherent) fluctuation component q_c and a random (incoherent) fluctuation component q_r (this is the so-called triple decomposition of a time signal, Reynolds and Hussain [19]), Fig. 5 presents a typical application of the phase-averaging method to the temperature signal $T(t)$: item (a) shows the normal velocity signal $v(t)$, item (b), the band pass filter output signal $v_f(t)$ and item (c), the distribution over a shedding period of the phase-averaged $T'(t)$, denoted by $\langle T' \rangle$. From now on, angular brackets $\langle\ \rangle$ will denote phase averaging.

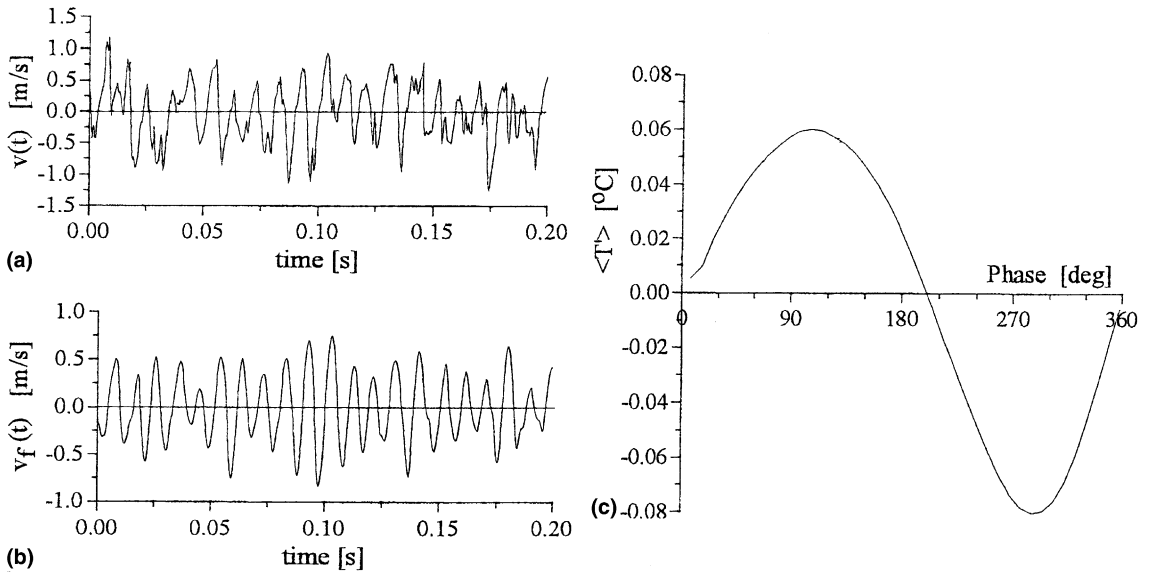

Fig. 5. (a) Normal velocity fluctuation signal $v(t)$, (b) band-pass filtered signal $v_f(t)$, derived from $v(t)$, (c) typical distribution over one shedding period of the phase-averaged temperature fluctuation.

The evaluation of the coherent and incoherent parts of the product of two fluctuating terms $qs(t)$ (q and s can be any of the terms $u(t)$, $v(t)$ and $T'(t)$) was carried out according to the following relations:

$$\text{coherent part of } qs(t) = q_c \cdot s_c, \tag{8}$$

$$\text{incoherent part of } qs(t) = \langle qs \rangle - q_c \cdot s_c = \langle q_r s_r \rangle. \tag{9}$$

3.3.2. Coherent flow contribution to conventionally averaged quantities

Following the isolation of the coherent flow by the method presented in the previous section, the proportion and hence, the significance of this motion compared to the conventionally time-averaged flow was investigated. For that reason, the coherent flow contributions to the global time-averaged values of the Reynolds stress components $\overline{u^2}$, $\overline{v^2}$, $\overline{uv}$, the temperature variance $\overline{T'^2}$ and the heat flux components of the $\overline{uT'}$ and $\overline{vT'}$ were determined by averaging over one shedding period the phase-averaged values of these parameters. The coherent quantities are denoted in general terms by $\overline{\overline{q_c s_c}}$ (e.g., coherent contribution to shear stress $= \overline{\overline{u_c v_c}}$).

Distributions of $\overline{qs}$ (the overall time-average) and $\overline{\overline{q_c s_c}}$ across the wake, normalized by the velocity defect U_d and the temperature excess T_e are presented in Figs. 6 and 7.

Fig. 6 shows that the coherent motion has a much larger contribution to $\overline{v^2}$ than to $\overline{u^2}$. Even at the furthermost measurement station ($x/D = 35$, Fig. 6(f)), $\overline{\overline{v_c^2}}$ is significant whereas the distribution of $\overline{\overline{u_c^2}}$ at the same station is almost negligible (Fig. 6(c)). It must be noticed here that since the reference signal in coherent structure education method has been derived from $v(t)$, the contributions to $\overline{u^2}$, $\overline{uv}$ and $\overline{uT'}$ are likely to be underestimated relatively to the contributions to $\overline{v^2}$ and $\overline{vT'}$. Therefore, the results presented in Figs. 6 and 7 should be viewed with this fact kept in mind.

Fig. 6(d)–(f) indicate a gradual immersion of the coherent motion in the boundary layer flow, as the $\overline{\overline{v_c^2}}$ distribution curves expand gradually to smaller values of y^+. Global and coherent shear stress distributions (Fig. 6(g)–(i)) have the same sign everywhere across the flow. Although the boundary layer–wake interaction causes major changes in $\overline{uv}$, the effect on $\overline{\overline{u_c v_c}}$ is relatively minor. Hence, it may be deduced that one of the primary effects of the interaction process is a significant weakening of the incoherent component in the lower half wake flow, associated with a substantial generation of incoherent flow in the boundary layer.

Distribution of the temperature variance $\overline{T'^2}$ and its coherent $\overline{\overline{T_c'^2}}$ across the wake indicates that heat is transferred mainly by the action of the incoherent flow (Fig. 7(a)–(c)). There is, however, a definite amount of heat moved by the coherent flow towards higher y^+ values also shown in Fig. 7(a)–(c). Coherent streamwise heat flux is present only together with the negative part of the global heat flux distribution (Fig. 7(d)–(f)). Global and coherent normal heat flux distributions have the same general shape and sign at all three measurement stations (Figs. 7(g)–(i)). They both expand continuously with streamwise distance towards higher y^+ values.

3.3.3. Topological features of the present flow field

Contour maps of various phase-averaged quantities associated with the coherent and incoherent components of the present flow are presented in this section. The con-

tour maps refer to the phase, $\varphi - y^+$ plane. The horizontal scale can be transformed from phase (i.e., time) to streamwise distance coordinates, since 2π corresponds to one wavelength $= U_v \cdot T_{st}$, where T_{st} is the Strouhal period and U_v is the convection velocity of the von Kármán vortices, taken equal to the value of mean velocity at the half velocity defect point [4]. The U_v values thus obtained at the measurement stations considered, are given in Table 1. Two vortex-shedding periods are displayed on the horizontal axis of each contour map for completeness. The phase scale is in reverse order, i.e., with increasing values from left to right in order to denote a flow direction in that sense. The same length scale has been used in both axes in order to represent the physical space correctly. Figs. 8(a)–(c) show the phase-averaged non-dimensional spanwise vorticity $\langle\omega\rangle D/U_d$ contours at the three measurement stations, determined from the following relation:

$$\langle\omega\rangle = \left(\frac{d(\overline{V} + v_c)}{dx} - \frac{d(\overline{U} + u_c)}{dy}\right). \tag{10}$$

Taylor's hypothesis has been used for the calculation of the streamwise gradient $d/dx \equiv -U^{-1}d/dt$. For the structure propagation velocity U, the present flow vortex convection velocity U_v was utilized, as suggested in the literature [4]. Since U_v was evaluated at each measurement station, a short time and distance validity of Taylor's hypothesis was thus assumed.

At the first measurement station, $x/D = 15$, Fig. 8(a) shows that there are discrete vortical structures behind the cylinder (the cylinder was located at $y^+ = 430$) with a specific distribution in space and time, typical of a von Kármán vortex street. Boundary layer vorticity does not appear to be influenced to any great extent by the presence of the vortex street. Hence, it may be assumed that the interaction process is still in an initial stage. At $x/D = 25$ (Fig. 8(b)) the same vortex organization is present. Peak vorticity have lower values compared to those at $x/D = 15$. Boundary layer vorticity has been generally increased everywhere near the surface. Furthermore, a local expansion of vorticity towards larger y^+ values can be observed at $\varphi = 0$ (and at $\varphi = \pm 360$) which may be seen as a boundary layer vorticity flux in the vertical direction. All the above events have been further developed at the last measurement station (Fig. 8(c)). The appreciable distortion of the coherent vortices between $x/D = 15$ and $x/d = 35$ should not be attributed to the interaction process exclusively, since vortex distortion has been observed and reported in the case of an isolated cylinder in cross-flow, as well [4]. The $\langle\omega\rangle D/U_d = \pm 0.65$ contours appear in dashed lines in all subsequent figures in order to mark the location of the vortices in the $\varphi - y^+$ plane.

Also shown in Figs. 8(d)–(f) are plots of the coherent velocity vector $\vec{U}_c$ defined as follows:

$$\vec{U}_c = (\overline{U} + u_c - U_v)i + (\overline{V} + v_c)j, \tag{11}$$

where i and j are unit vectors along the x-axis and the y-axis, respectively. $\overline{V}$ is very small in the present flow and it has been neglected in the calculations. The main topological features of the present coherent flow field can be observed in Fig. 8(d): the location of adjacent large-scale vortices (typical of a von Kármán vortex street, as mentioned earlier), the position of the structure centers (denoted by letters c) and the position of the saddle points (denoted by letters s). As implied by Eq. (11), the frame of reference moves with velocity U_v, following the coherent structures motion. Hence, the free-stream flow ($y^+ > 650$) appears to move faster, and the boundary layer flow ($y^+ < 200$) appears to move slower. In Figs. 8(e)–(f), although the topological features mentioned above are present in the upper half-wake (on the free-stream side), they are missing in the lower half-wake, especially in Fig. 8(f). This is attributed to the fact that as the wake–boundary layer interaction proceeds in the streamwise direction, the traveling speed of the vortices in the lower half-wake decreases. Hence, in a reference frame that follows the motion of the upper half-wake vortices, the appearance of the lower half-wake vortices is obscured.

Fig. 9 presents contours of the phase-averaged streamwise and normal velocity components, normalized by U_d. The appearence of the contours in the wake region is similar to that reported for the case of an isolated cylinder in cross-flow [4,16]. The interaction with the boundary layer seems to create a very limited distortion of the contours at low y^+ values ($y^+ < 300$) in the form of an extension towards the surface, without any marked effects of particular importance.

The same comments, in general, apply to Figs. 10(a)–(f). These figures show contours of the phase-averaged coherent and random shear stress components in normalized form. Furthermore, it may be observed that peak values of random (incoherent) shear stress in the lower half-wake decrease with x/D much more rapidly than peak values in the upper half-wake (Figs. 10(d)–(f)). On the contrary, $-\langle u_r v_r\rangle$ within the boundary layer increases very rapidly with streamwise distance. It is reminded here that this behavior was first observed in Figs. 6(g)–(i) (Section 3.3.2), where it was attributed to the wake–boundary layer interaction process which apparently had a much more significant effect on the random flow than on the coherent flow. It may be added here that according to the coherent structures model behind a cylinder in cross-flow, proposed by Hussain and Hayakawa [4], $-\langle u_r v_r\rangle$ contours are associated and aligned with the primary mechanism for random turbulent kinetic energy production, termed the "ribs". The interaction process in the present flow appears to have a significant effect on the ribs in the lower half-wake and consequently, on the turbulent kinetic energy production in that region. This issue has been investigated in a separate work. Related results have been published in a paper by Sideridis et al. [20].

3.3.4. Heat transport results

All experimental results related to the distribution and transport of heat in the present flow fields are shown in Figs. 11 and 12. First, contour plots of the normalized coherent temperature fluctuations T_c'/T_e at the three measurement stations appear in Figs. 11(a)–(c). It is evident that discrete hot and cold regions exist in the $\phi - y^+$ plane that grow rapidly with x/D. It is reminded here that the terms hot and cold refer to temperatures higher and lower, respectively, than the local mean temperature. Each shedding period is divided in two halves: one predominantly hot, located at $0° < \phi < 180°$ and another, predominantly cold, located at $180° < \phi < 360°$. Both regions expand faster in the y^+ direction than in the ϕ-direction. The hot region in each shedding period seems to be associated with the up-going alleyway between adjacent vortices (refer to Figs. 8(d)–(f)). Similarly, the cold region seems to be associated with the down-going alleyway. These facts imply that the coherent motion transferred hot fluid behind the heat source upwards, away from the surface and cold fluid downwards, towards the surface. Both these motions appear to have been implemented by the combined action of positive and negative vorticity.

Figs. 11(d)–(f) show contour maps of the coherent streamwise heat flux component. At the first measurement station (Fig. 11(d)), $u_c T_c'/U_d T_e$ has very small magnitude and it is limited to the area behind the line heat source ($y^+ \approx 150$). In each shedding period, two discrete regions with negative values are present. Their peak values are considerably larger further downstream, reaching a maximum at $x/D = 25$. Both regions expand with streamwise distance in both ϕ- and y^+-directions. Furthermore, two new regions, both with positive $u_c T_c'/U_d T_e$ values, appear in each shedding period at $x/D = 25$ and expand on the $\phi - y^+$ plane with x/D.

Each half-shedding period in Figs. 11(d)–(f) contains a large negative region and, at locations downstream of $x/D = 15$, two additional positive regions. Considering now the fact that the first half of each shedding period is associated with hot fluid and the second half with cold fluid (as deduced from Figs. 11(a)–(c)), the direction of the coherent streamwise heat flux may be determined as follows. In the first half period, in the region of negative $u_c T_c'$, u_c is negative (since T_c' is positive) and in the region of positive $u_c T_c'$, u_c is positive. In the second half period, in the region of negative $u_c T_c'$, u_c is positive (since T_c' is negative) and in the region of positive $u_c T_c'$, u_c is negative. (These results may be verified from the plots in Figs. 9(a)–(c)).

The appearance of the coherent normal heat flux contour plots (Figs. 12(d)–(f)) is similar to the corresponding contour plots of the streamwise heat flux, presented in Figs. 11(d)–(f). In each half-shedding period, there is one main region of positive $v_c T_c'$ values. Associating these regions with the discrete regions of hot and cold fluid in Figs. 12(a)–(c), it is concluded that hot fluid moves upwards ($v_c T_c' > 0$, $T_c' > 0$, hence $v_c > 0$) through the up-going alleyway between adjacent vortices. Cold fluid moves downwards ($v_c T_c' > 0$, $T_c' < 0$, hence $v_c < 0$) through the down-going alleyway (refer to Figs. 9(d)–(f) and Figs. 8(d)–(f)). Also present in each half-shedding period there is a small region with much lower negative $v_c T_c'$ values, (except at $x/D = 35$, where this region has become too small to be shown). Associating again these regions with the corresponding regions of the T_c' contour plots (Figs. 11(a)–(c)), it can be deduced that at $0° < \phi < 180°$ the negative $v_c T_c'$ region denotes an upward motion of cold fluid ($v_c > 0$, $T_c' < 0$) through the thermal wake of the line heat source (located at $y^+ = 150$). At $180° < \phi < 360°$ the negative $v_c T_c'$ region denotes a downward motion of hot fluid ($v_c < 0$, $T_c' > 0$).

All results obtained from Figs. 11 and 12 regarding the direction of heat transport have been utilized in Fig. 13 to create a schematic presentation of the coherent motion of hot and cold fluid in relation to the large-scale coherent structures of the present flow. It is implied in Fig. 13 that the frame of reference moves with the coherent structure transport velocity U_v. Consequently, hot fluid orginating from the thermal wake region, approaches structure A in an *upstream* direction. Close to that structure, the hot fluid direction changes to *downstream*, following the rotational motion imposed by the structure. Cold fluid (i.e., fluid at ambient temperature) is driven downwards, through the thermal wake, under the combined action of structures A and C. It may be noticed in Fig. 13 that although the cold fluid motion covers the whole down-going alleyway between vortices A and C, as deduced from Figs. 11 and 12, hot fluid is directed preferentially to vortex A where it may be argued that it is "captured" by the vortical motion.

It is also noted that the aforementioned kind of motion of low-momentum fluid in the upward direction is dominant in the near-wall region (ejections, [13]) of an undisturbed boundary layer. Hence, a close relationship is envisaged between the events taking place in the near-wall region of the present boundary layer and the coherent flow. In a similar way, cold fluid observed in the present flow moving towards the plate through the alleyway between adjacent coherent structures in the wake, ought to relate at some location near the plate to the strong movement of high-momemtum fluid towards the wall (sweeps, [13]) present in an undisturbed boundary layer.

The data presented in Figs. 11 and 12 indicated two additional motions in the coherent flow field close to the surface: (a) hot fluid moving towards the surface, which is presumably part of the cold fluid mentioned above and which is heated as it passes through the thermal wake, and (b) cold fluid being driven away from the surface, through the thermal wake, contributing to the up-going hot fluid discussed above.

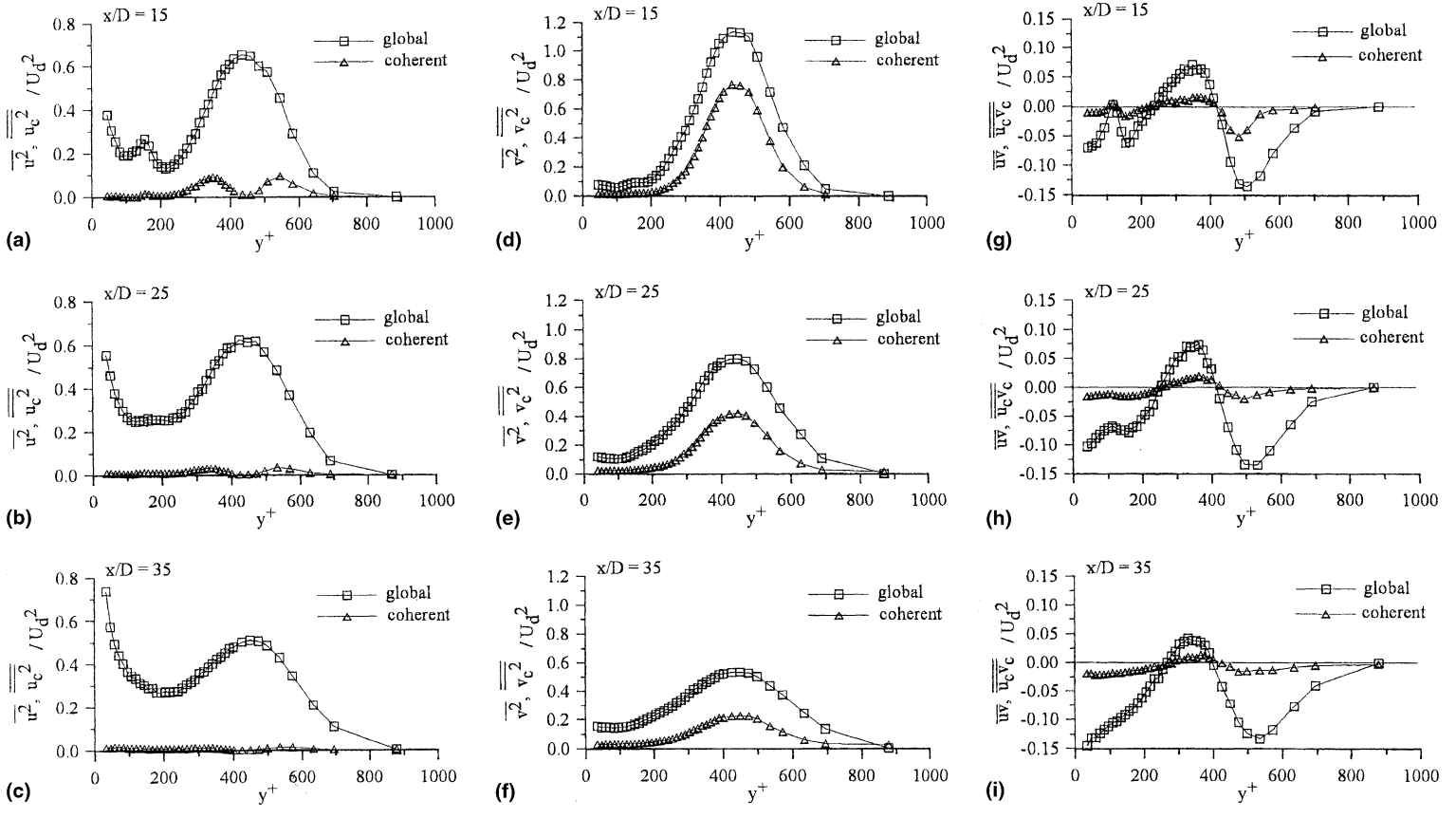

Fig. 6. Distributions of the global and coherent normal stresses and temperature variance normalized by the velocity defect U_d and the temperature excess T_e.

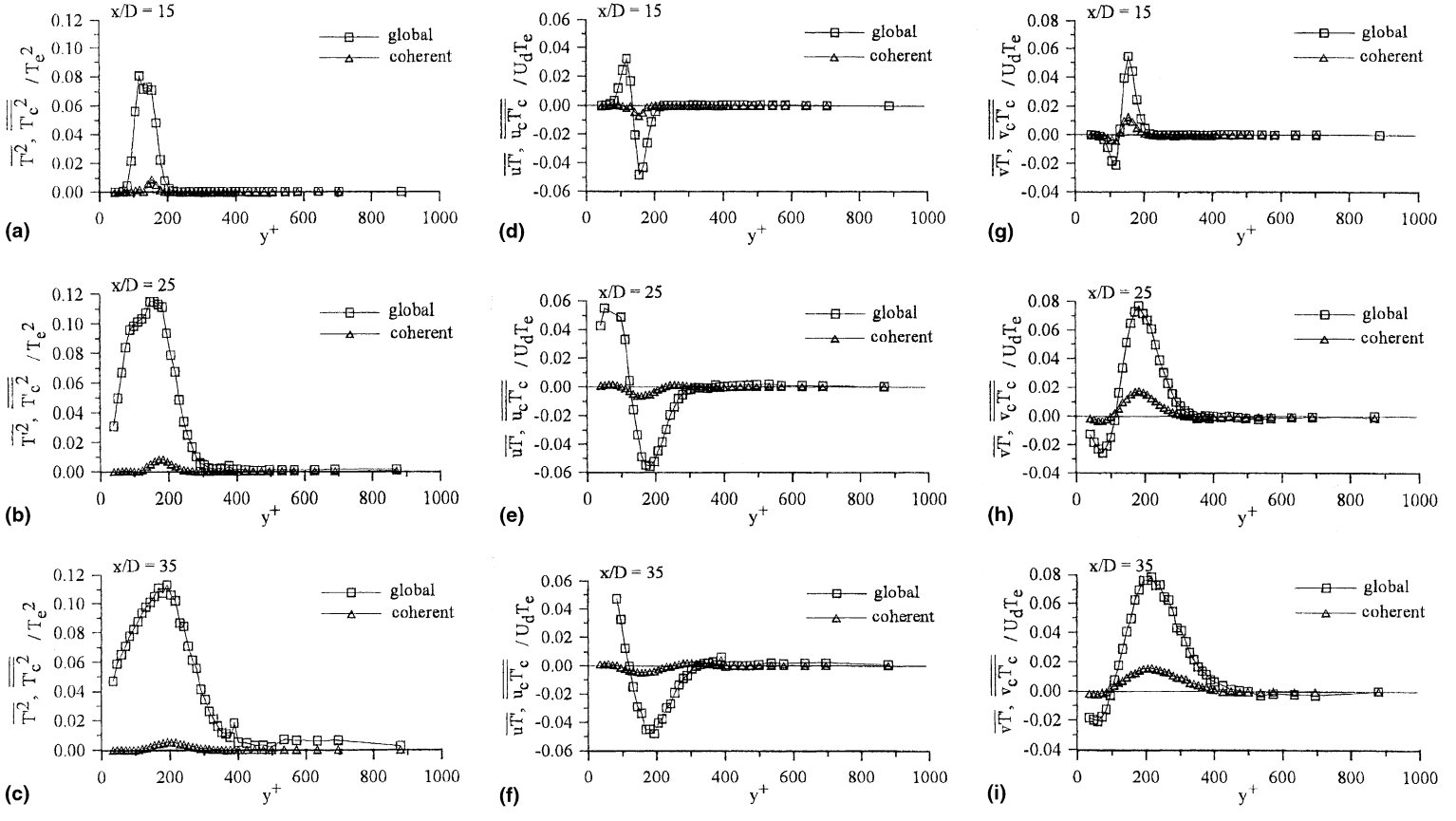

Fig. 7. Distributions of the global and coherent shear stresses and heat flux components normalized by the velocity defect U_d and the temperature excess T_e.

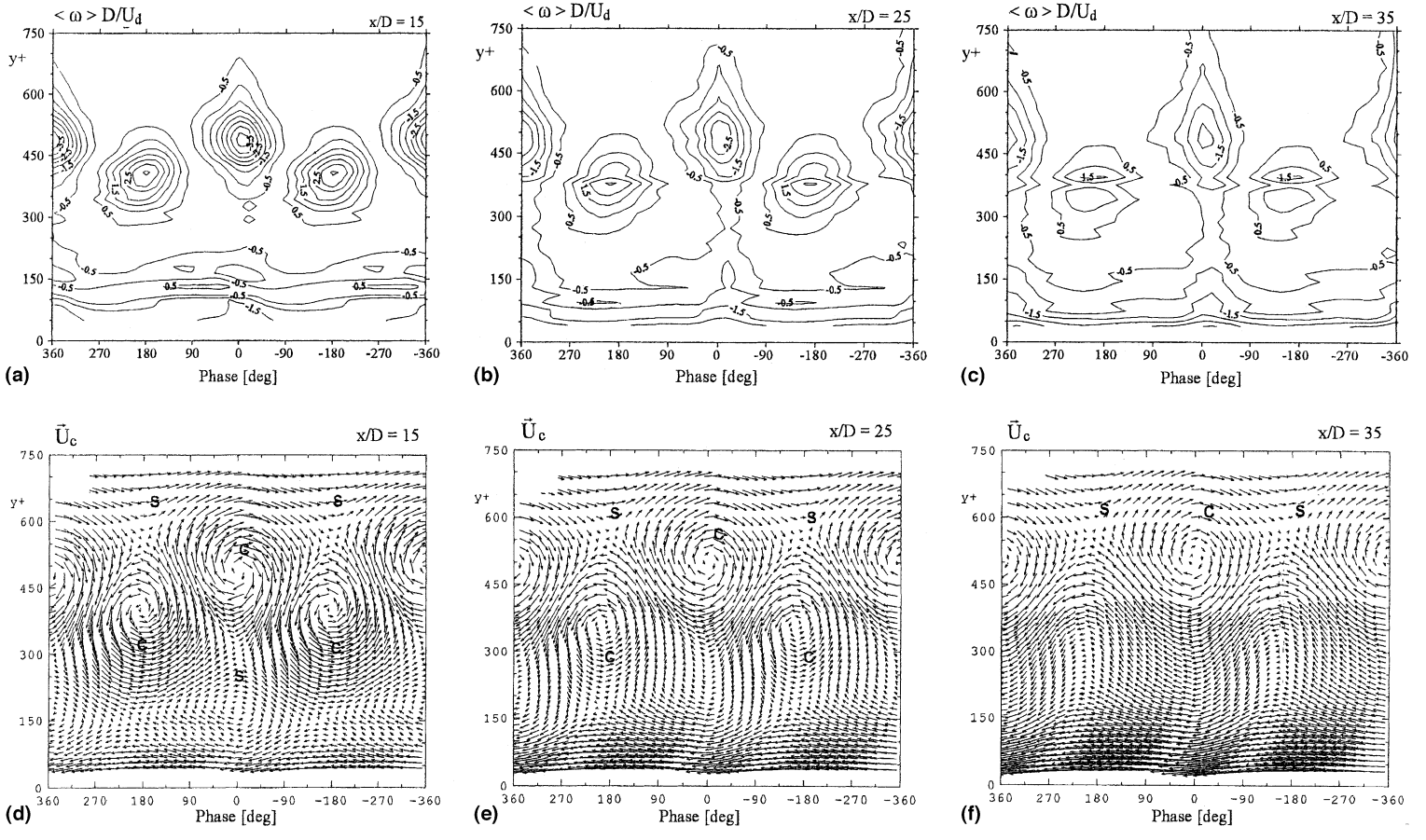

Fig. 8. (a)–(c) Contour maps of the phase-averaged spanwise vorticity, at $x/D = 15$, 25, 35, respectively. (d)–(f) Corresponding vector plots of phase-averaged velocity at the same x/D-locations. c: Structure centers, s: saddle points. Frame of reference moves with the convection velocity of the coherent vortices. In all diagrams, flow direction is left to right. The cylinder is located at $y^+ = 430$.

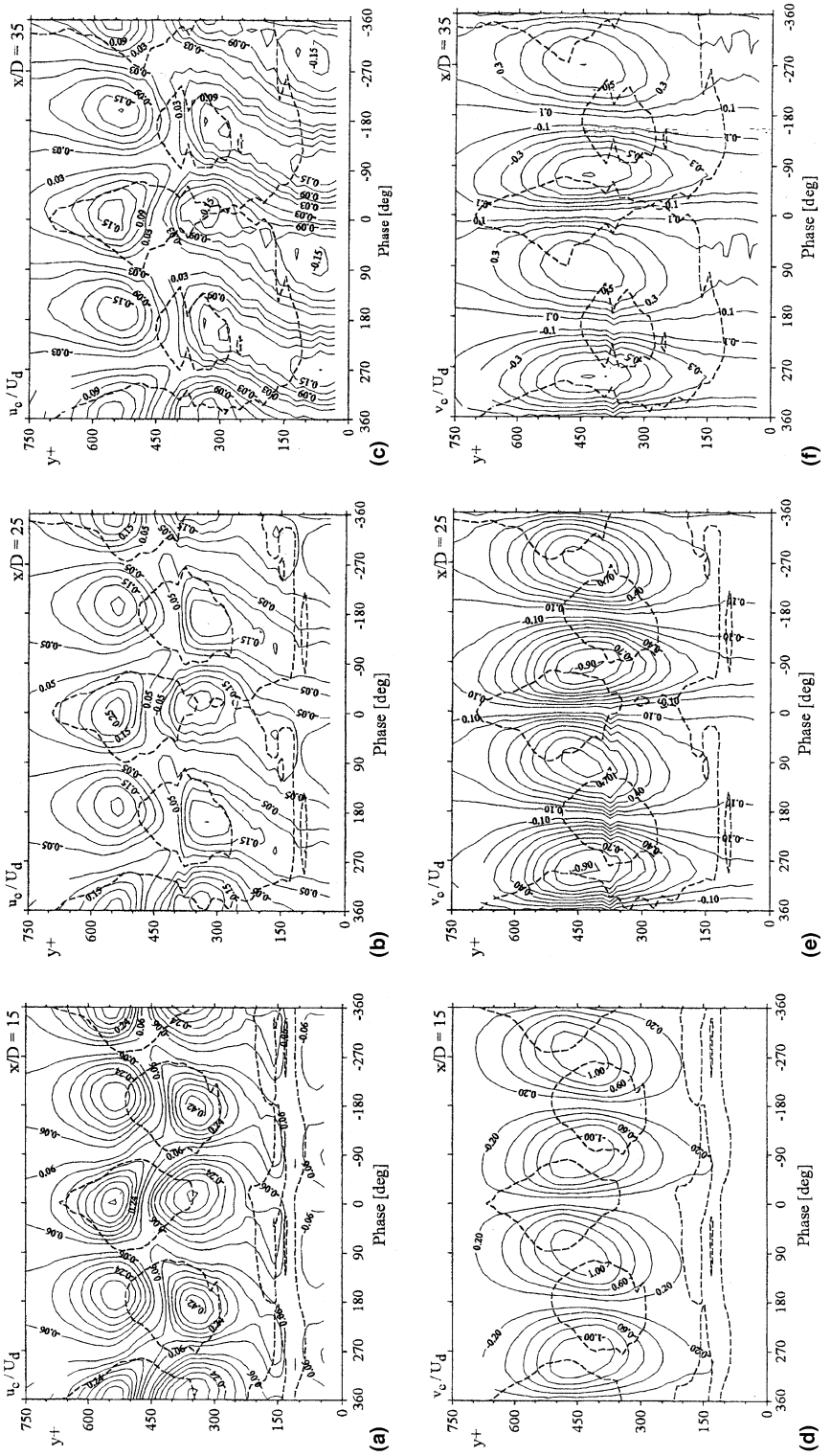

Fig. 9. Contour maps of the phase-averaged streamwise and vertical velocity components u_c, v_c.

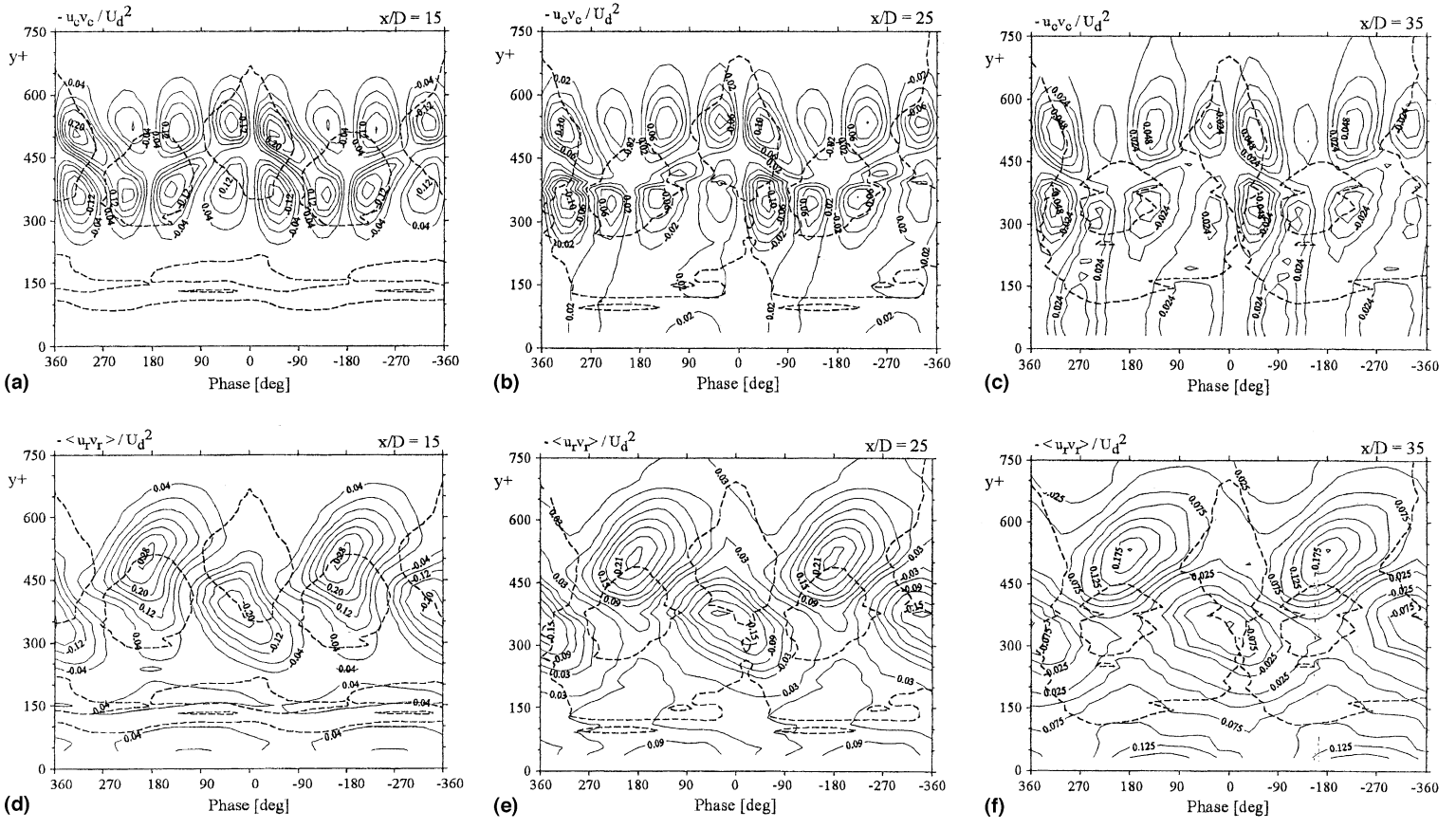

Fig. 10. Contour maps of the phase-averaged coherent and incoherent shear stress components $-u_c v_c$, $-\langle u_r v_r \rangle$.

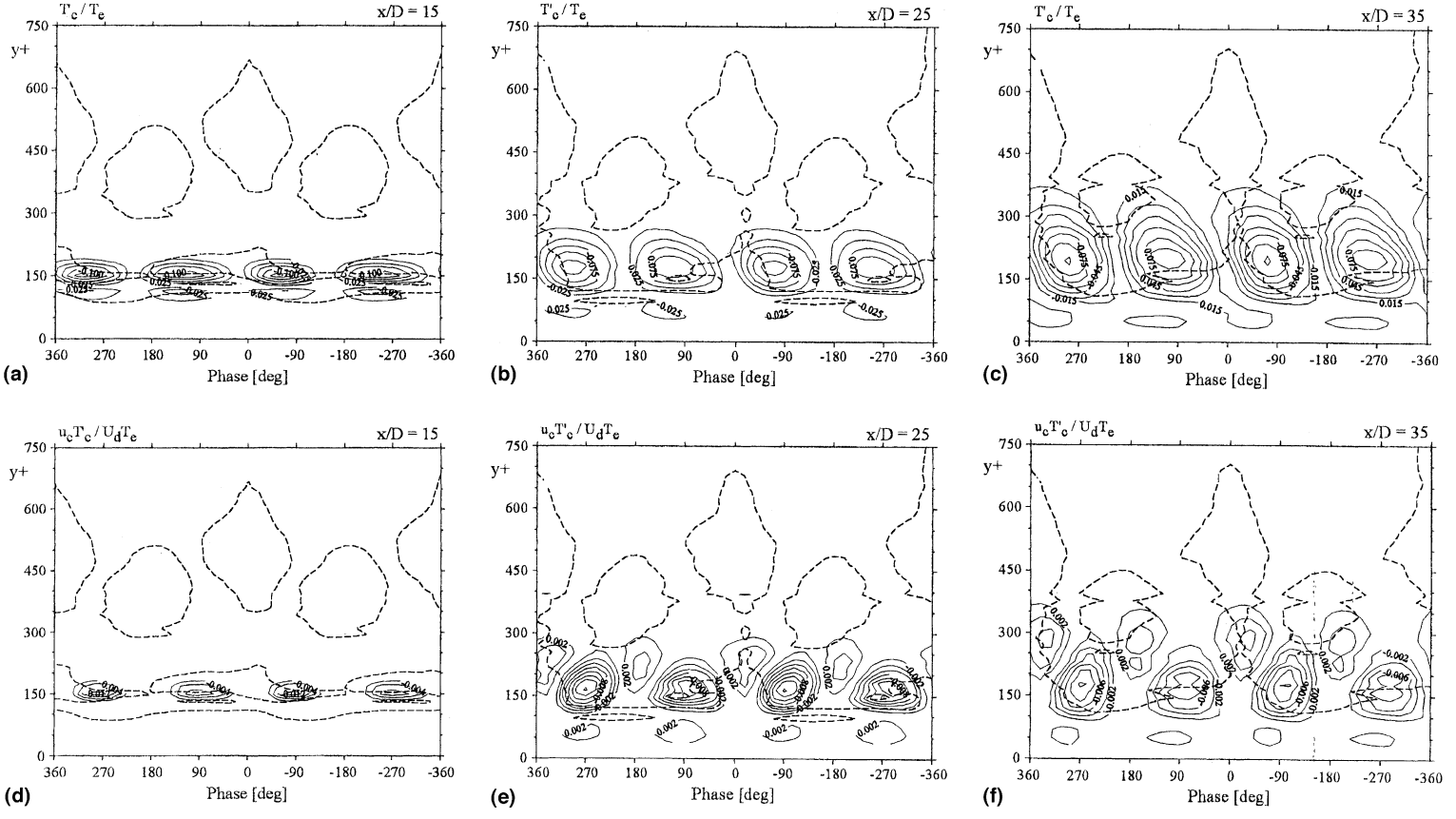

Fig. 11. Contour maps of the phase-averaged coherent temperature fluctuations T_c' and the coherent streamwise heat flux component $u_c T_c'$.

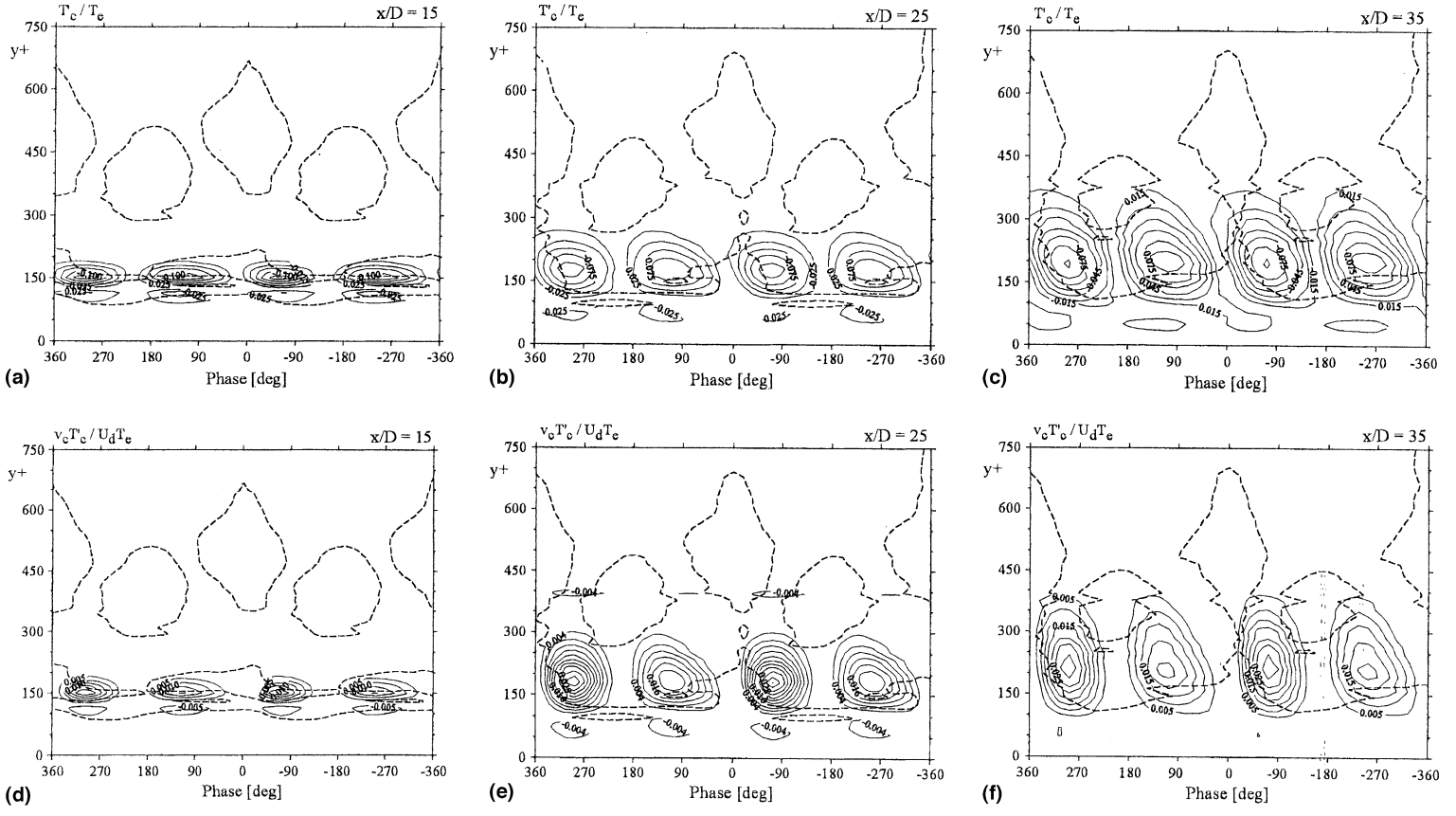

Fig. 12. Contour maps of the phase-averaged coherent temperature fluctuations T_c' and the coherent normal heat flux component v_cT_c'.

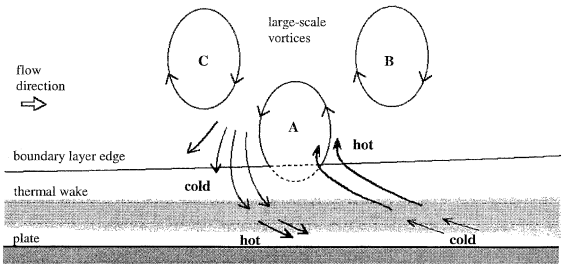

Fig. 13. Schematic presentation of the coherent motion of hot and cold fluid relative to the large-scale coherent structures. Frame of reference moves with the structures convection velocity.

4. Conclusions

The analysis of the present experimental data based on a phase-averaging technique has provided valuable insight into the coherent flow field structure and the associated heat transport mechanisms of the present flow. Large-scale coherent vortices with a strongly periodic organization and enhanced quasi two-dimensional characteristics were identified in the flow. Their interaction with the adjacent boundary layer affected mainly the lower part of the vorted street and in particular, its incoherent flow component. Only one particular motion in the coherent flow field was found to transport hot fluid, the motion directed from the plate towards the lower half-wake vortices at a streamwise velocity lower than the local time-mean velocity.

Hot fluid reaching the vicinity of the lower half-wake vortices pursued their vortical motion. This fact may be interpreted as entrapment of hot fluid by the coherent vortices. Since this is a continuously developing process in the streamwise direction, the implication is that scalar accumulation should be expected which might reach significant levels. In a real situation, e.g., an industrial accident involving leakage of a harmful substance, coherent structures in the atmosphere may create locally dangerous concentrations of that substance.

In the present work, only the initial stages of the entrapment process were examined. Further research focused on the evolution of this process would be very useful.

Acknowledgements

The present work was supported by the European Communities Commission. Contract No. AVI-CT92-0017.

References

[1] J.J. Turner, Turbulent entrainment: the development of the entrainment assumption and its application to geophysical flows, J. Fluid Mech. 173 (1986) 431–471.

[2] S.J. Lin, G.M. Corcos, The mixing layer: deterministic models of a turbulent flow, Part 3. The effect of plane strain on the dynamics of streamwise, J. Fluid Mech. 141 (1984) 139–178.

[3] A.K.M.F. Hussain, Coherent structures and turbulence, J. Fluid Mech. 173 (1986) 303–356.

[4] A.K.M.F. Hussain, M. Hayakawa, Eduction of large-scale organized structures in a turbulent plane wake, J. Fluid Mech. 180 (1987) 193–229.

[5] K. Suzuki, H. Suzuki, V. Kikkawa, H. Kigawa, Study on a turbulent boundary layer disturbed by a cylinder-effect of cylinder size and position, in: Proceedings of the Seventh Symposium on Turbulent Shear Flows, Stanford University, 1989, pp. 8.5.1–8.5.6.

[6] F. de Souza, J. Delville, J. Lewalle, J.P. Bonnet, On the large scale organization of a turbulent boundary layer distributed by a circular cylinder, in: Proceedings of the Eleventh Symposium on Turbulent Shear Flows, Grenoble, France, 1997, pp. 33.25–33.30.

[7] T.L. Doligalski, C.R. Smith, D.A. Walker, Vortex interactions with walls, Annu. Rev. Fluid Mech. 26 (1994) 573–616.

[8] F.S. Chuang, A.T. Conlisk, The effect of interaction on the boundary layer induced by a convected rectilinear vortex, J. Fluid Mech. 200 (1989) 337–365.

[9] A. Luton, S. Ragab, D. Telionis, Interaction of spanwise vortices with a boundary layer, Phys. Fluids 7 (11) (1995) 2757–2765.

[10] R.H. Kraichnan, Inertial ranges in two-dimensional turbulence, Phys. Fluids 10 (1967) 1417–1423.

[11] H. Tennekes, Turbulent flow in two and three dimensions, Bull. Am. Meteorol. Soc. 59 (1978) 22–28.

[12] G.A. Sideridis, E.G. Kastrinakis, S.G. Nychas, Experimental simulation of air pollution dispersion by atmospheric motions, in: H. Powel, et al. (Eds.), Proceedings of the Air Pollution III Conferene, vol. 2, Computational Mechanics Publications, Boston, Southampton, 1995, pp. 177–184.

[13] G.A. Sideridis, E.G. Kastrinakis, S.G. Nychas, Conditional analysis of turbulent heat transport in a quasi two-dimensional wake interacting with a boundary layer, Int. J. Heat Mass Transfer 42 (1999) 3481–3494.

[14] F.R. Hama, An efficient tripping device, J. Aero. Sci. 24 (1957) 236–237.

[15] P.N. Papanikolaou, J.N.E. Papaspyros, E.G. Kastrinakis, S.G. Nychas, A fast digital technique for calibration of hot-wires over a wide temperature range, Meas. Sci. Technol. 8 (1997) 1363–1366.

[16] M. Matsumura, R.A. Antonia, Momentum and heat transport in the turbulent intermediate wake of a circular cylinder, J. Fluid Mech. 250 (1993) 651–668.

[17] Jayesh, C. Tong, Z. Warhaft, On temperature spectra in grid turbulence, Phys. Fluids 6 (1994) 306–312.

[18] M. Kiya, M. Matsumura, Incoherent turbulence structure in the near wake of a normal plate, J. Fluid Mech. 190 (1988) 343–356.

[19] W.C. Reynolds, A.K.M.F. Hussain, The mechanisms of an organized wake in turbulent shear flow, Part 3. Theoretical models and comparisons with experiments, J. Fluid Mech. 54 (1972) 263–288.

[20] G.A. Sideridis, E.G. Kastrinakis, S.G. Nychas, Turbulence production and transport in quasi two-dimensional wake/boundary layer interaction, AIAA J. 38 (2) (2000) 259–266.